

UNIVERSITÀ DEGLI STUDI DI NAPOLI,
FEDERICO II

CORSO DI LAUREA MAGISTRALE IN INGEGNERIA
DELL'AUTOMAZIONE E ROBOTICA

Field aNd Service Robotics: homework 4

Studente: Ciro Manfredonia

Matricola: P38000291

Docente: Fabio Ruggiero

GitHub Link:

https://github.com/ciromanfry/FSR_Homework4_Ciro_Manfredonia.git

May 2025

1 Buoyancy effect.

The buoyancy effect is a hydrostatic phenomenon that must be taken into account for underwater robots. It is referred to as hydrostatic since it occurs even when the robot is stationary, either underwater or at the surface, and it depends on the fluid density ρ , the norm of the gravitational acceleration g , and the volume of the body submerged in the fluid Δ .

The buoyancy force acts at the center of buoyancy, which may not coincide with the robot's center of mass, where the gravitational force acts. In such cases, a torque can be generated that affects the stability of the robot underwater, as the buoyancy force tends to push the robot upward toward the surface, while the gravitational force tends to pull it downward toward the bottom.

For this reason, one of the design requirements should be to align the center of mass and the center of buoyancy along the same vertical line.

This effect should be considered for any robot moving in a fluid. However, in aerial robotics, it is often neglected because the density of air is much lower compared to that of the robot itself. In contrast, for underwater robots, the density of water is comparable to that of the robot, so the buoyancy effect becomes significant and must be taken into account.

2 Briefly justify whether the following expressions are true or false.

a) FALSE.

This expression is false because the added mass effect does not imply a real increase in the robot's physical mass. In reality, when the robot accelerates in water, it also accelerates the surrounding fluid particles due to the reactive forces generated by its motion through the fluid. This interaction results in an additional inertial effect, which is interpreted as an added mass. However, no actual mass is physically added to the robot.

b) TRUE.

The second sentence is true because, for underwater robots, the density of the surrounding fluid, the water, is comparable to the density of the robot itself. This is why the added mass effect becomes significant. In contrast, for aerial robots flying through air, the effect is negligible since the density of air is much lower than that of the UAV.

c) TRUE.

The third sentence is true due to the presence of fluid viscosity, which causes dissipative drag forces that oppose the robot's forward (heading) velocity, and lift forces that oppose its vertical (up and down) motion. Damping is often modeled using a positive definite matrix D_{RB} that scales the body's velocity. When employing Lyapunov stability theory with a candidate function V derived from the system's kinetic energy, the time derivative \dot{V} includes a velocity-dependent quadratic term involving D_{RB} , which ensures dissipation and contributes to improved system stability.

d) **FALSE.**

The sentence is false because the ocean current effect, modeled as a velocity contribution that influences the motion of the robot, is considered constant and irrotational with respect to the world frame. However, when referred to the body frame, this effect should be treated as time-varying.

3 Quadruped Simulation.

In the third exercise, we were required to complete the whole-body control scheme for the quadruped by defining the function that solves the quadratic optimization problem, yielding the optimal values of the desired ground reaction forces f_{gr}^* and the desired joint accelerations \ddot{q}_j^* , in order to command the robot using different types of gaits.

The Quadratic problem could be expressed as

$$\begin{aligned} \min_{\zeta} \quad & f(\zeta) \\ \text{s.t.} \quad & A\zeta = b \\ & D\zeta \leq c \end{aligned} \tag{1}$$

In which the vector of control variable is $\zeta = [\ddot{r}_c^T \quad \ddot{q}_j^T \quad f_{gr}^T]^T \in \mathbb{R}^{n_b+n_j+3n_{st}}$ and where $r_c = [p_c^T \quad \eta_c^T]^T$.

The quadratic optimization problem is addressed using the qpSWIFT solver, a tool specifically developed for fast and efficient quadratic programming.

```
[zval, basic_info, adv_info] = qpSWIFT(sparse(H), g, sparse(Aeq),
                                         beq, sparse(Aineq), bineq);
```

Where the matrices A_{eq} , A_{ineq} and vectors b_{eq} , b_{ineq} define the equality and inequality constraints of the problem.

The variable `zval` contains the optimal solution to the quadratic programming (QP) problem, providing the control inputs that minimize the objective function while satisfying all constraints.

Once the desired command values for the quadruped are computed, the main idea is to leverage the differences between various gaits, which primarily differ in the motion of the four legs. These differences manifest in terms of position, heading velocity, angular velocity, and ground reaction force tracking.

In the initial simulations, all parameters were kept at their default values, where the desired velocity is $v_d = 0.5 \text{ m/s}$, the mass is $m = 5.5 \text{ kg}$, and the friction coefficient is $\mu = 1$.

3.1 Trot gait

The trot gait enables the quadruped robot to move by alternating the motion of diagonal leg pairs. While two legs are in the swing phase, the remaining two stance legs form a support polygon that effectively reduces to a single line. In order to analyze the gait, the following plots were produced.

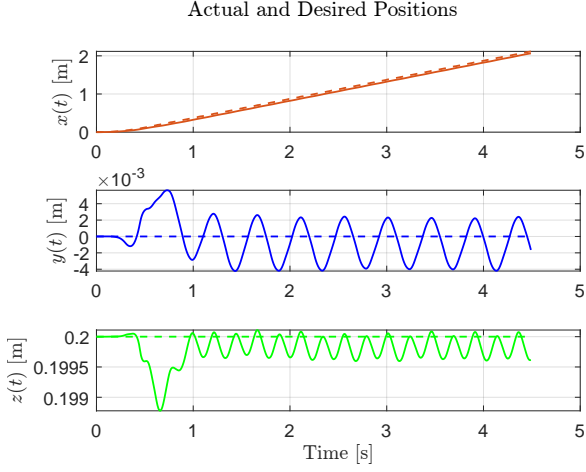


Figure 1: position with trot gait

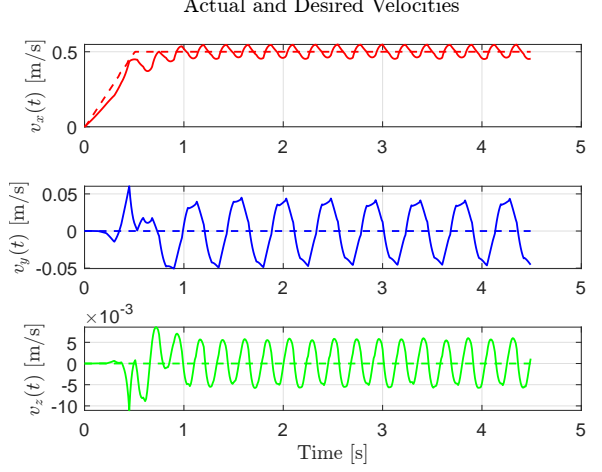


Figure 2: velocity with trot gait

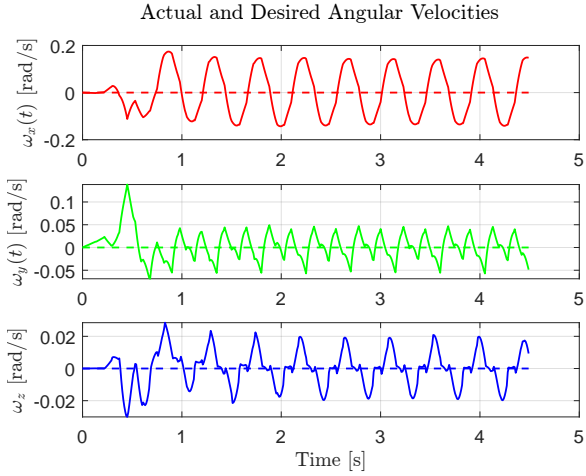


Figure 3: angular velocity with trot gait

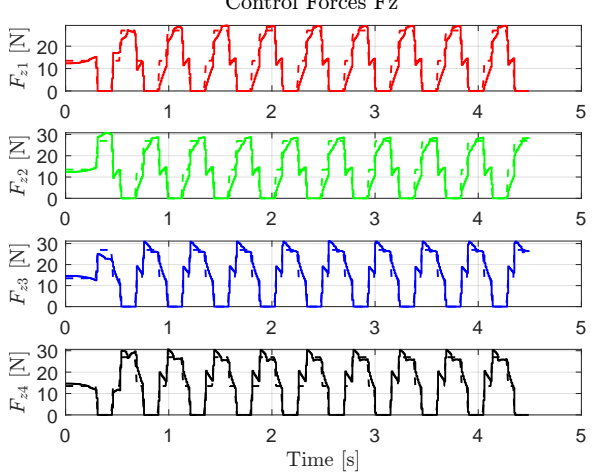


Figure 4: GRF with trot gait

From the plots above, we can observe that the tracking error along the x-axis is negligible, whereas the positions along the y and z-axes exhibit oscillations around the desired values. These fluctuations are primarily due to the alternating motion of the diagonal legs during the trot gait, which causes the robot's torso to tilt. The gait also affects the heading and the angular velocities along the x, y, and z axes, causing the velocities to oscillate around the desired values.

From the ground reaction forces plot, we can observe the effective alternation of the diagonal legs, highlighting time intervals during which all four legs are in stance. The maximum value of the ground reaction forces remains within 30 N for all the four legs. Since the robot's final snapshot from the simulation does not offer additional insights, it will be excluded from the analysis.

However, all simulation videos will be accessible through the GitHub repository.

[Click here to download and view the simulation video of the trot gait.](#)

3.2 Bound gait

The bound gait enables the quadruped robot to move by simultaneously swinging either the front or the rear legs, while avoiding a phase where all four legs are in contact with the ground at the same time.

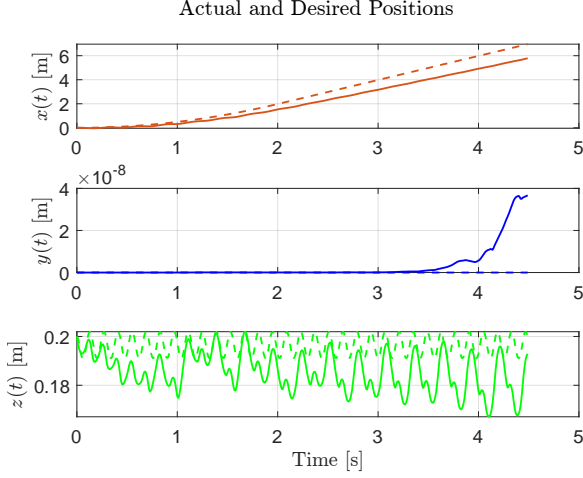


Figure 5: position with bound gait

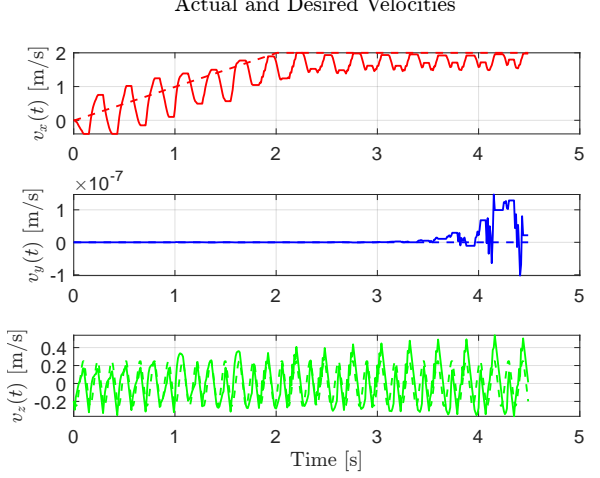


Figure 6: velocity with bound gait

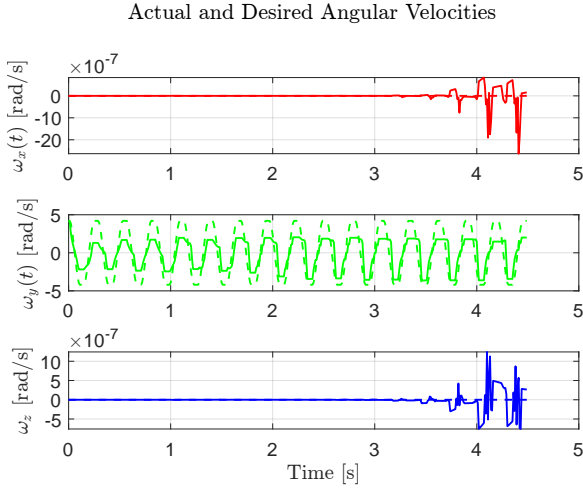


Figure 7: angular velocity with bound gait

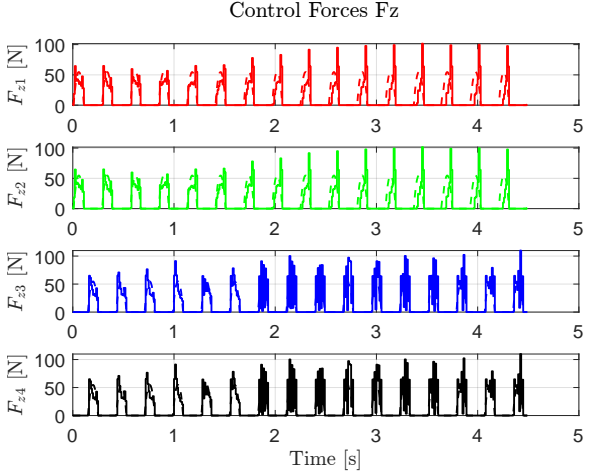


Figure 8: GRF with bound gait

As we can see from the plots, the position error has increased compared to the previous gait, but the actual distance traveled by the quadruped has also grown. Another interesting aspect to note is that the velocity along the x -axis initially oscillates around the desired value. During the transient phase, it tends to remain below the desired value, eventually reaching a peak equal to the target velocity.

With this gait, the ground reaction forces reach up to 100 N, highlighting that the front legs alternate their movement with the hind legs, supporting the robot's entire weight on only two legs for brief intervals, and vice versa, without all four legs ever being in contact with the ground simultaneously.

[Click here to download and view the simulation video of the bound gait.](#)

3.3 Pacing gait.

The pacing gait involves the lateral legs moving in coordination, enabling the robot's forward motion.

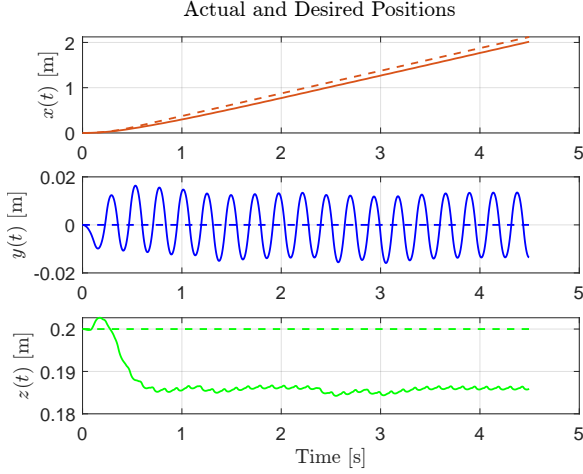


Figure 9: position with pacing gait

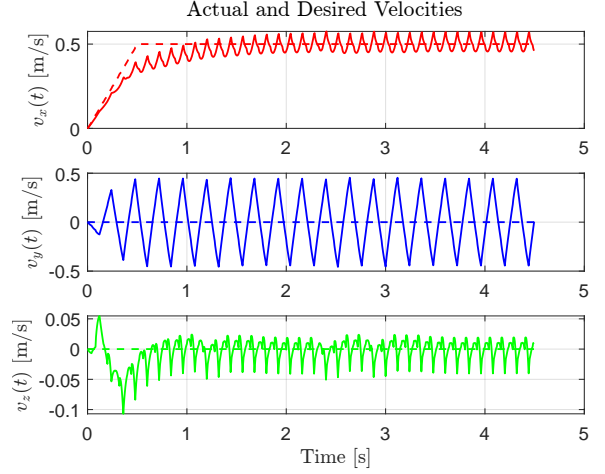


Figure 10: velocity with pacing gait

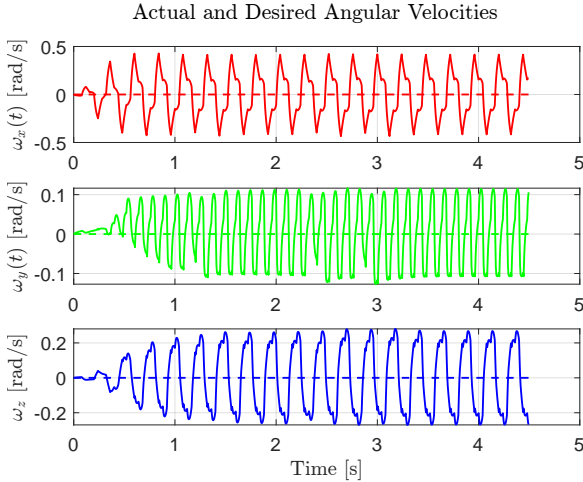


Figure 11: angular velocity pacing gait

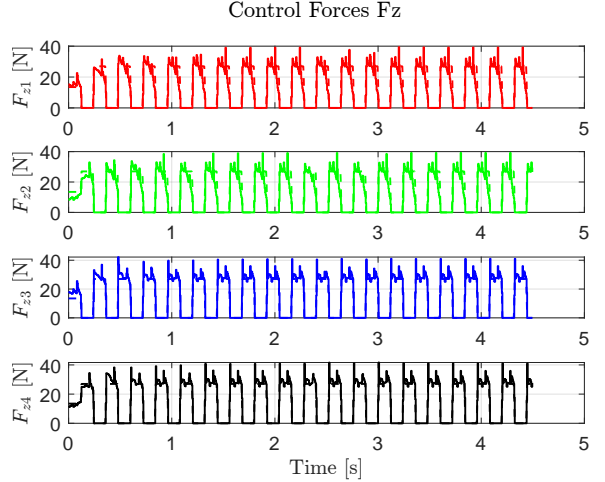


Figure 12: GRF with pacing gait

The position error along the x-axis decreases compared to the previous case but is still worse than in the trot gait. For the y and z axes, the position oscillates around the desired values because the robot tilts to ensure that the projection of the center of mass lies within the support polygon, which in this gait reduces to a line connecting the two lateral legs alternately. This phenomenon can also be observed in the plots of heading and angular velocities, where oscillations are clearly evident. The ground reaction forces decrease to a magnitude of approximately 40 N.

[Click here to download and view the simulation video of the pacing gait.](#)

3.4 Gallop gait

In the gallop gait, motion is enabled by the alternating movement of the legs, with phases where only one leg is in stance at a given time. This gait is highly unstable, as there are few moments of multi-leg support—only a single foot remains in contact with the ground.

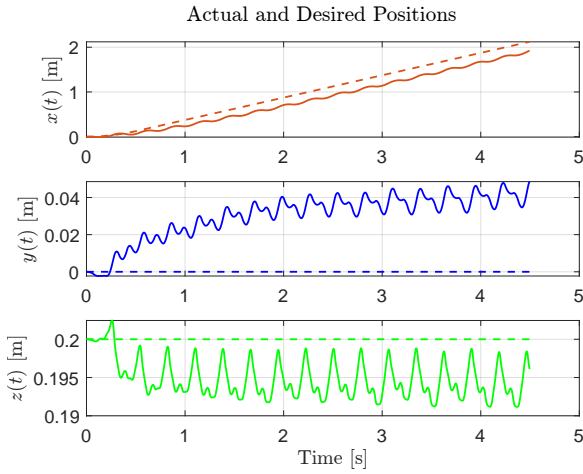


Figure 13: position with gallop gait

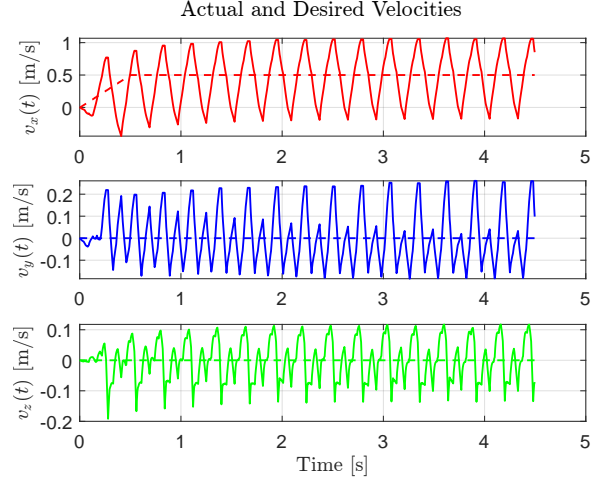


Figure 14: velocity with gallop gait

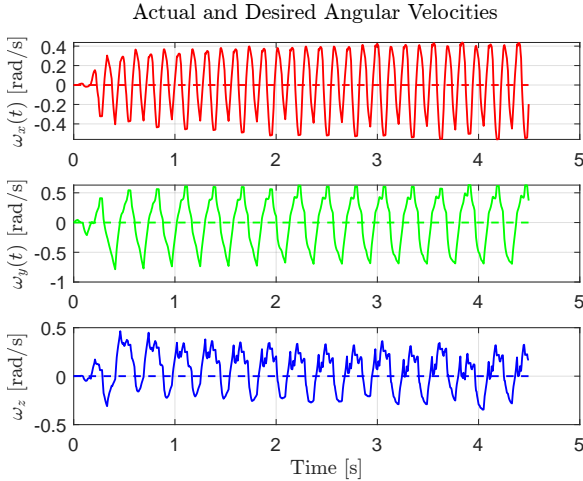


Figure 15: angular velocity gallop gait

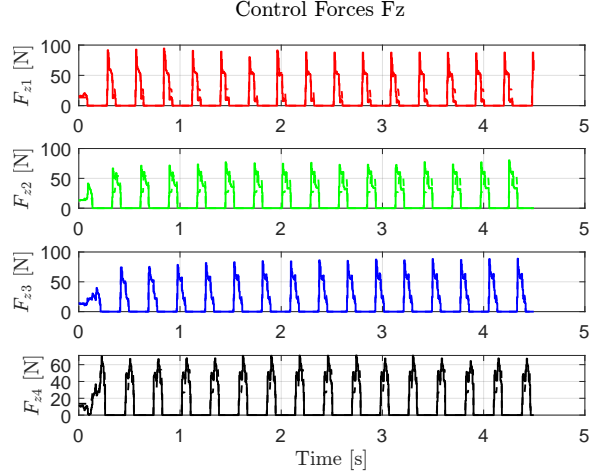


Figure 16: GRF with gallop gait

The gallop gait exhibits one of the highest heading velocities observed so far, oscillating and reaching a peak value of 1m/s. The position error along the x-axis is comparable to that of the pacing gait. Meanwhile, the positions along the y and z axes oscillate around the desired values. The y-axis position generally exceeds and diverges, causing an undesired torso orientation, while the z-axis position tends to fall below the target, due to the alternating stance legs. From the ground reaction forces, we can observe that each stance foot remains in contact with the ground for only a very short duration, and occasionally there are two feet simultaneously in contact. The ground reaction forces are high and comparable to those in the bound gait, reaching values up to 100 N.

[Click here to download and view the simulation video of the gallop gait.](#)

3.5 Trot run gait

This gait is very similar to the trot one, but in this case, all four legs never contact the ground simultaneously.

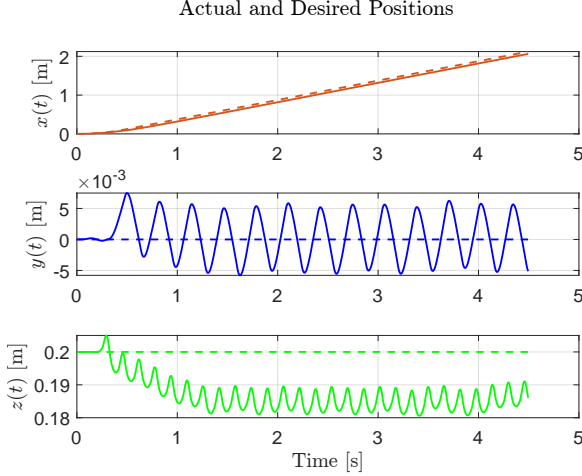


Figure 17: position, gallop run gait

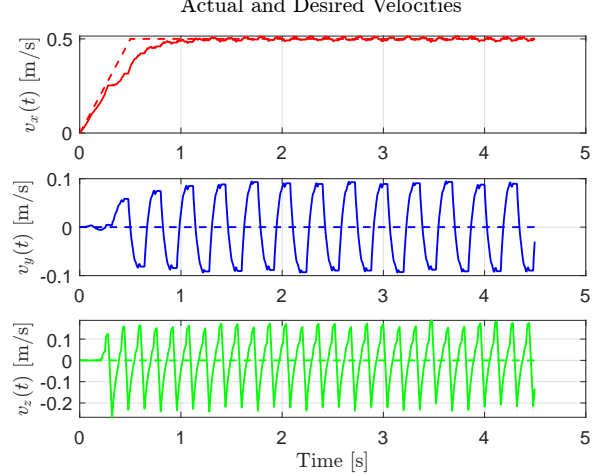


Figure 18: velocity, gallop run gait

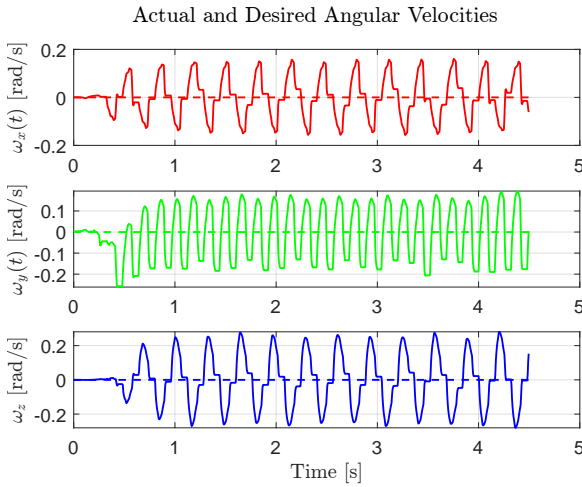


Figure 19: angular velocity, trot run gait

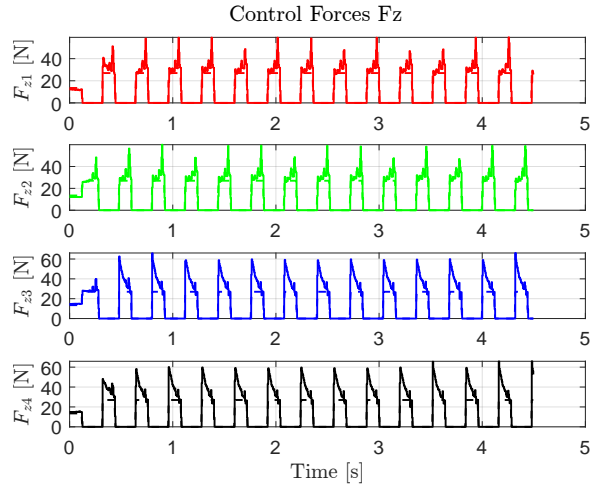


Figure 20: GRF, trot run gait

The evolution of the quadruped using the trot-run gait is quite comparable to that of the trot gait. However, the main differences concern the ground reaction forces, which increase up to a magnitude of 60 N due to the distribution of the quadruped's mass over a reduced number of legs; the tracking position along the z -axis, which remains consistently below the desired value and exhibits oscillations; and the resulting angular velocity around the z -axis, which increases in magnitude.

[Click here to download and view the simulation video of the trot run gait.](#)

3.5.1 Crawl gait

This gait offers the highest level of stability, as three legs remain in contact with the ground at all times, creating a triangular support polygon.

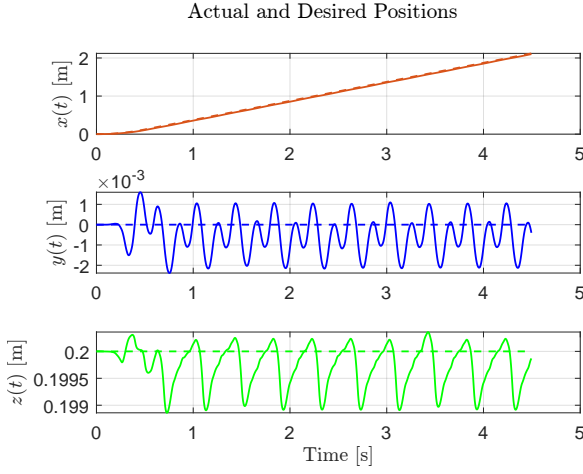


Figure 21: position with crawl gait

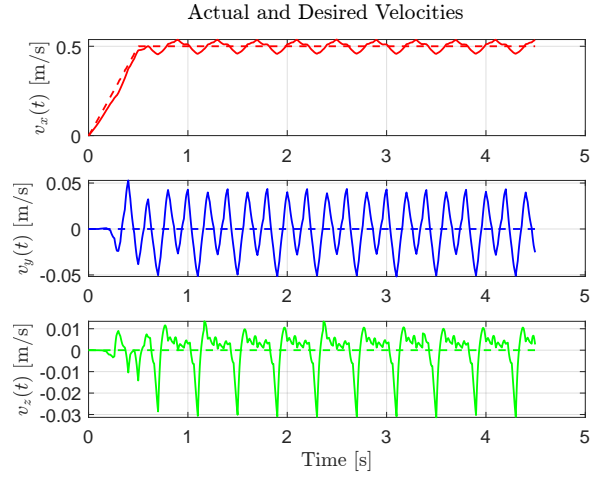


Figure 22: velocity with crawl gait

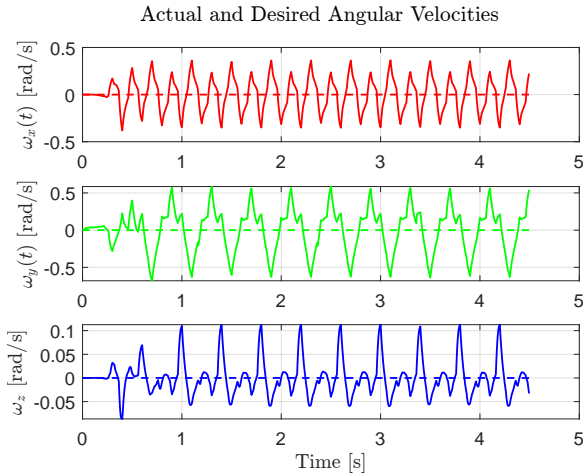


Figure 23: angular velocity with crawl gait

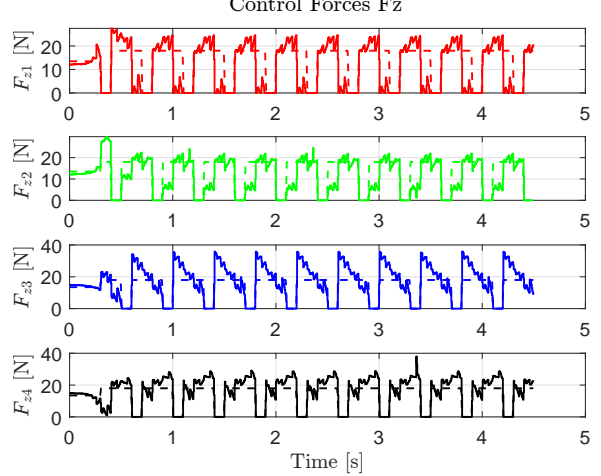


Figure 24: GRF with crawl gait

Analyzing the plot, it can be observed that at each instant, three legs are in stance phase, ensuring greater stability and maintaining ground reaction forces mostly below 30 N. An exception is found in the left hind leg, which reaches a peak reaction force of 40 N. From the position plot, it is evident that the tracking along the x -axis is highly accurate, while small oscillations are present along the y and z axes. These deviations correspond to minor fluctuations in the heading and angular velocities, which oscillate around their desired values.

[Click here to download and view the simulation video of the crawl gait.](#)

3.6 System behaviour under changes in the desired velocity.

As required by the exercise, one of the objectives was to increase the quadruped's desired velocity v_d and compare the resulting behaviour across different gaits. In the simulations, the desired velocity was set to $v_d = 1.2 \text{ m/s}$.

To streamline the analysis, only the best and worst solutions—based on selected parameters—will be presented, allowing for a focused evaluation of the optimal trot under

specific environmental conditions or parameter choices. Nevertheless, the plots from all simulations are saved in the `plots_mod` folder within the `fcs` folder.

After comparing all the simulations, it was found that the crawl gait provided the best performance in tracking the desired position, while maintaining the oscillations in heading and angular velocities close to the desired values. Compared to the previous case, in which the velocity was significantly lower, the ground reaction forces reach magnitudes of up to 60 N across all legs.

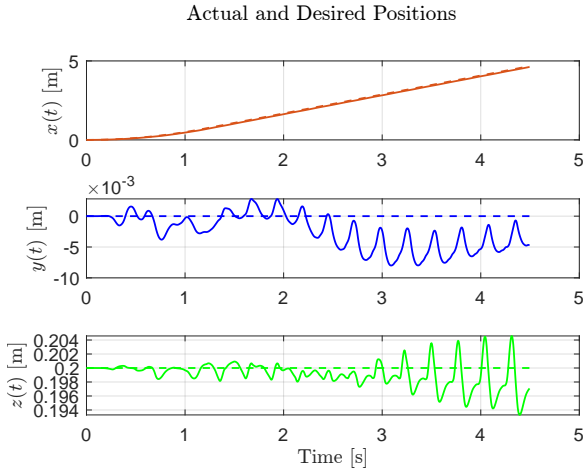


Figure 25: position with crawl gait

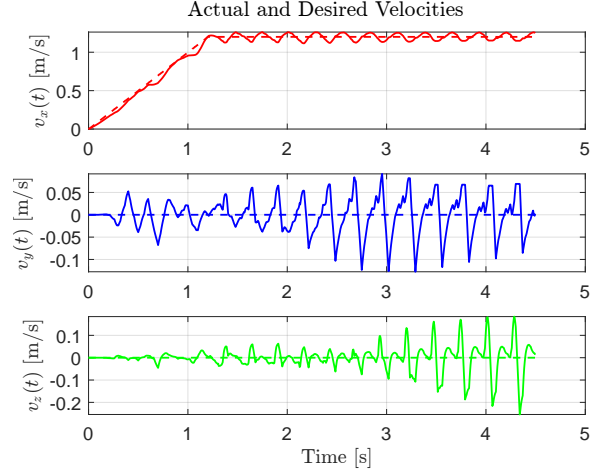


Figure 26: velocity with crawl gait

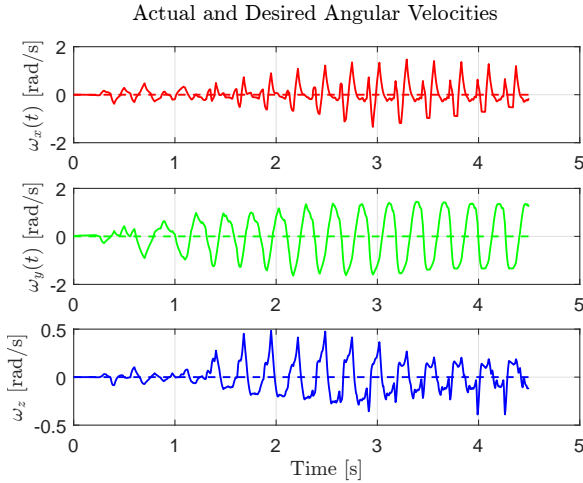


Figure 27: angular velocity with crawl gait

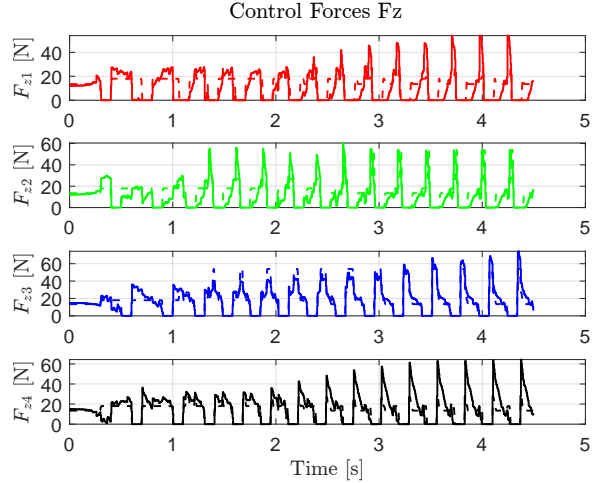


Figure 28: GRF with crawl gait

[Click here to download and view the simulation video of the crawl gait.](#)

Meanwhile, the worst performance was observed with the gallop gait.

As shown in the plot, after a few seconds the robot's orientation along the y -axis deviates significantly from the desired value, while the tracking along the x -axis shows only a slight deviation. Along the z -axis, oscillations below the desired position can be observed, which are caused by the positioning of the legs.

In this gait, the ground reaction forces are considerably higher, mainly due to the rapid transitions between stance and swing phases.

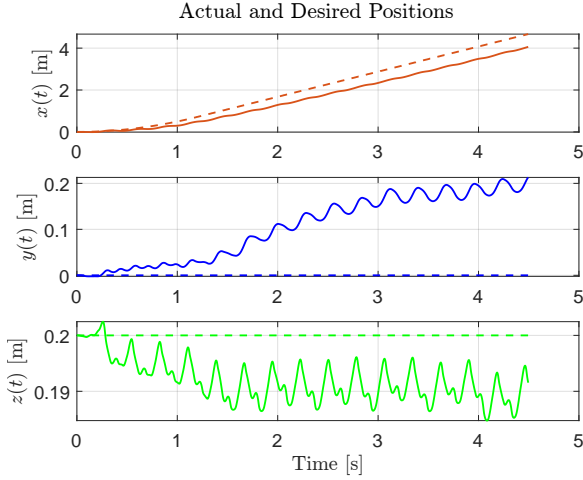


Figure 29: position with gallop gait

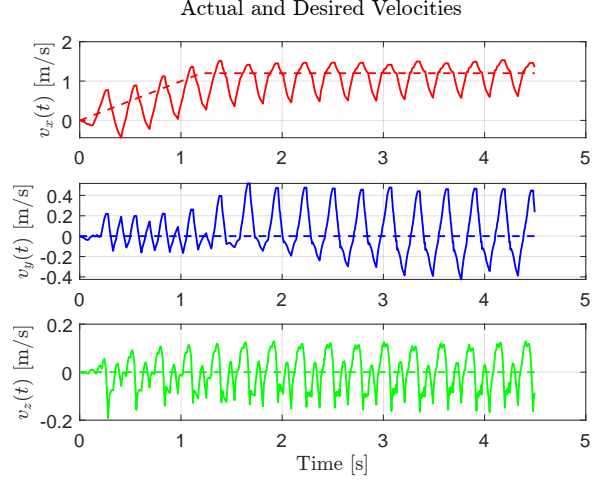


Figure 30: velocity with gallop gait

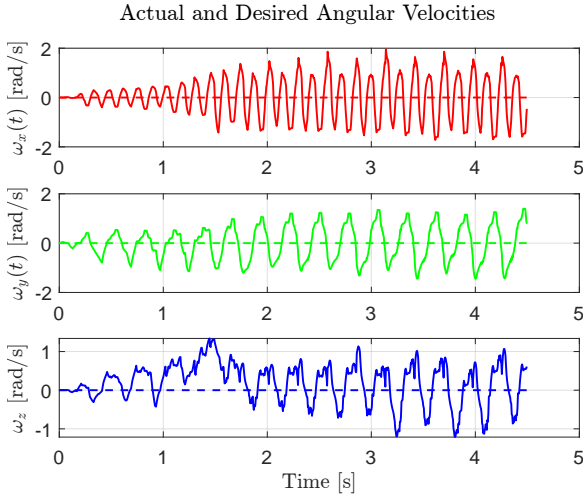


Figure 31: angular velocity gallop gait

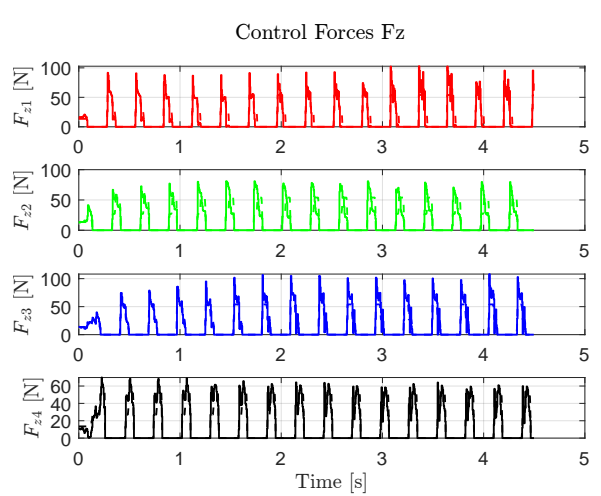


Figure 32: GRF with gallop gait

[Click here to download and view the simulation video of the gallop gait.](#)

3.7 System behaviour under variations in the friction coefficient and robot mass.

For the final case, the goal was to test extreme conditions and evaluate both the best and worst-case scenarios. The simulations were conducted with a desired velocity of $v_d = 1 \text{ m/s}$, a friction coefficient of $\mu = 0.2$, and an additional load mass of 1 kg attached to the robot.

Not all gaits were able to successfully perform the tracking task; In fact, the bound, pacing, and gallop gaits exhibited unfeasible behaviour.

Among all the unfeasible gaits, the pacing gait is analyzed in detail, as it exhibits the worst performance.

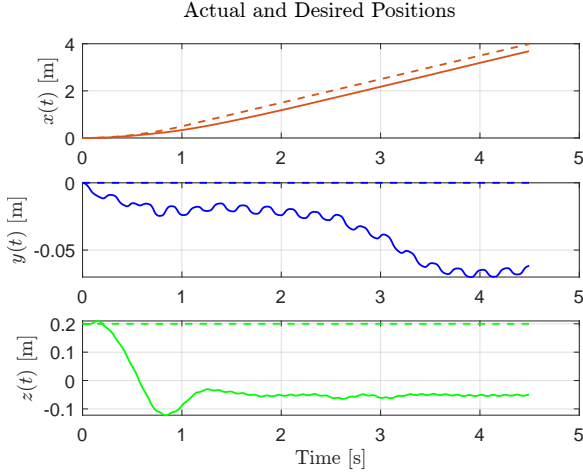


Figure 33: position with pacing gait

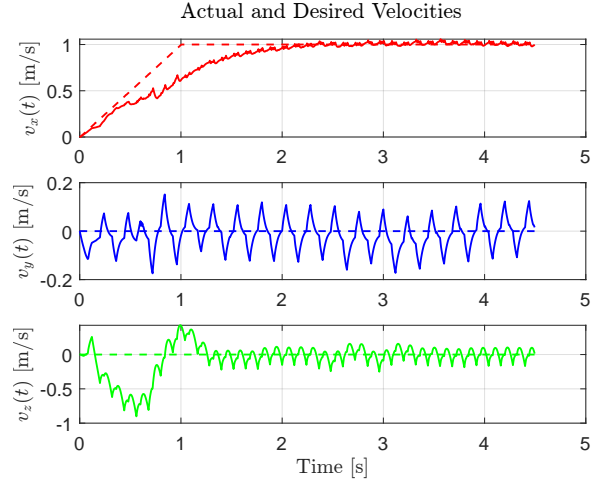


Figure 34: velocity with pacing gait

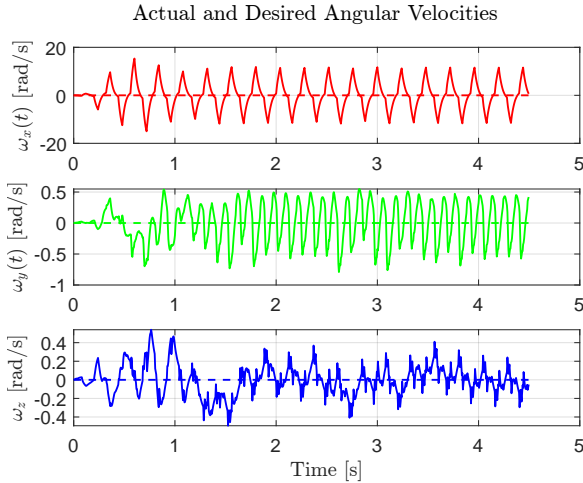


Figure 35: angular velocity pacing gait

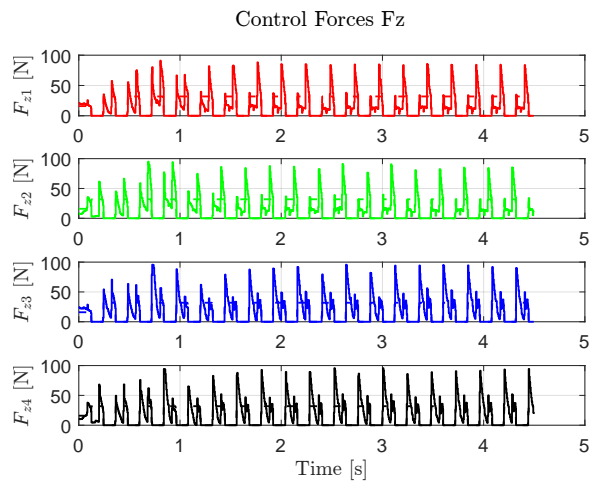


Figure 36: GRF with pacing gait

As shown in the position plots, the robot's torso—and therefore its center of mass—drops below ground level just a few seconds after the start of the simulation. This gait stands out among the unfeasible cases as the one in which the robot sinks below the ground level most rapidly, making the task clearly unrealizable in a real-world scenario. In this case, the increased mass and friction coefficient caused the robot's legs to lose traction depending on the gait pattern. Consequently, the robot was unable to successfully complete the task due to insufficient grip and stability during locomotion.

[Click here to download and view the simulation video of the pacing gait.](#)

Another gait that should be mentioned among those that failed to complete the task is the gallop gait. In the simulation, the robot can be seen falling and rotating around its own axis in an attempt to recover the desired orientation, while consistently remaining above the ground.

[Click here to download and view the simulation video of the gallop gait.](#)

Meanwhile, from the feasible gaits the one that performs better still remain the crawl gait.

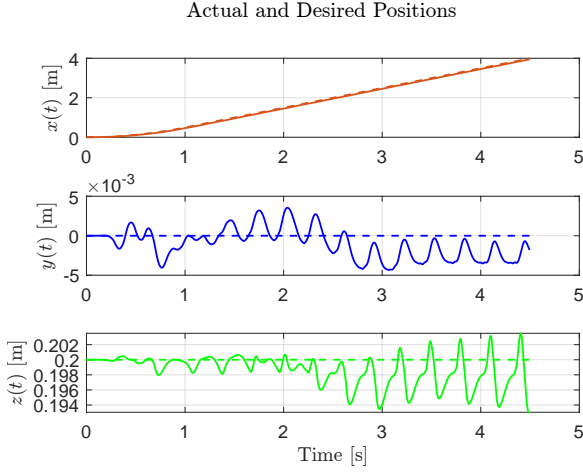


Figure 37: position with crawl gait

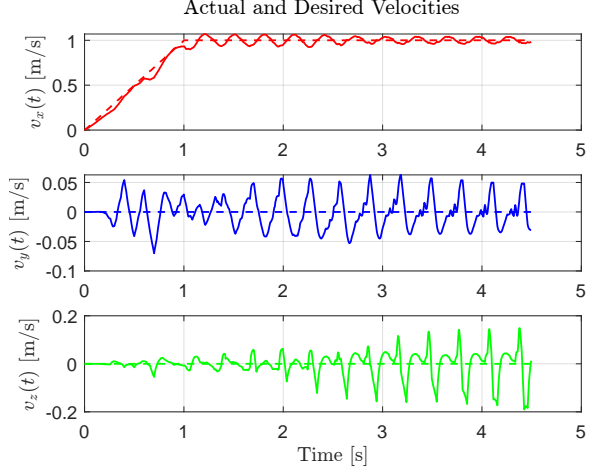


Figure 38: velocity with crawl gait

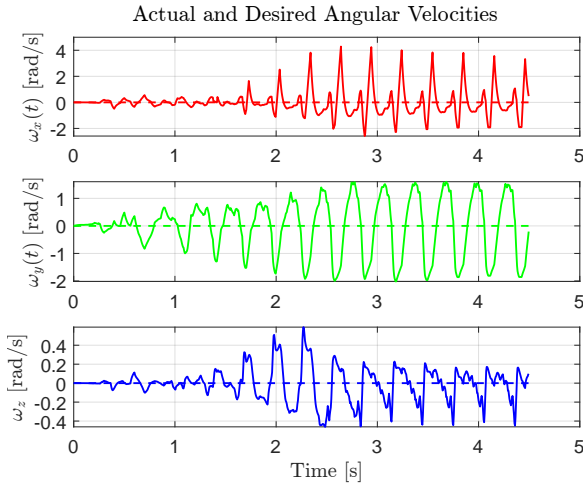


Figure 39: angular velocity with crawl gait

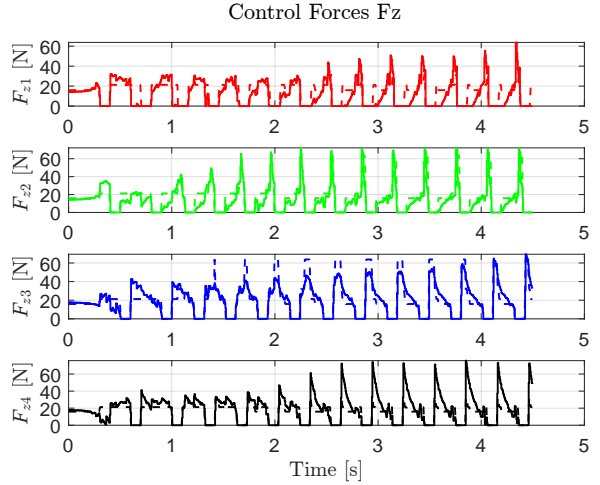


Figure 40: GRF with crawl gait

The position tracking along all axes performs very well, especially along the x -axis. In contrast, the y - and z -axes show only small-magnitude oscillations around the desired values. The overall stability—guaranteed by the fact that three feet are always in contact with the ground, as shown in the ground reaction forces plot where the GRF peaks at 60 N—is also reflected in the heading and angular velocities, which closely follow the reference values while oscillating around them.

In conclusion, for all the three cases analyzed, the crawl gait proved to be the most effective, as it adapts best to parametric variations of the initial conditions.

[Click here to download and view the simulation video of the crawl gait.](#)

4 Rimless wheel

Starting with an initial value of $\dot{\theta}_0 = 0.95$, a stable equilibrium point is identified at coordinates $(-0.3127, 0)$.

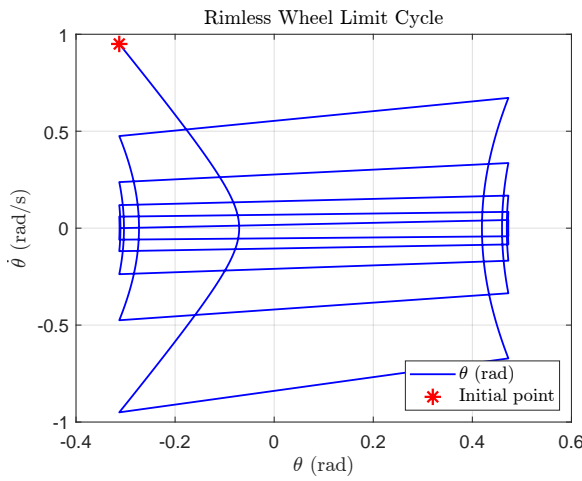


Figure 41: $\dot{\theta}_0 = 0.95$ and $p_i = (-0.31, 0.95)$

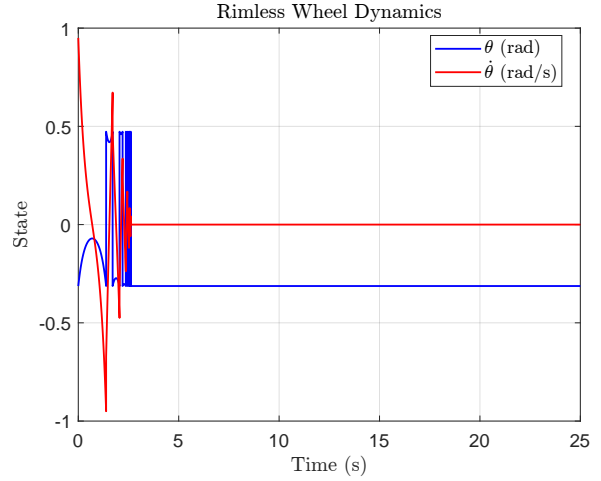


Figure 42: $\dot{\theta}_0 = 0.95$ and $p_i = (-0.31, 0.95)$

To investigate the system's behavior under varying initial angular velocities, a script was developed to systematically vary $\dot{\theta}_0$ and observe the resulting dynamics. The analysis distinguishes between positive and negative values of $\dot{\theta}_0$, which correspond to different equilibria of the system.

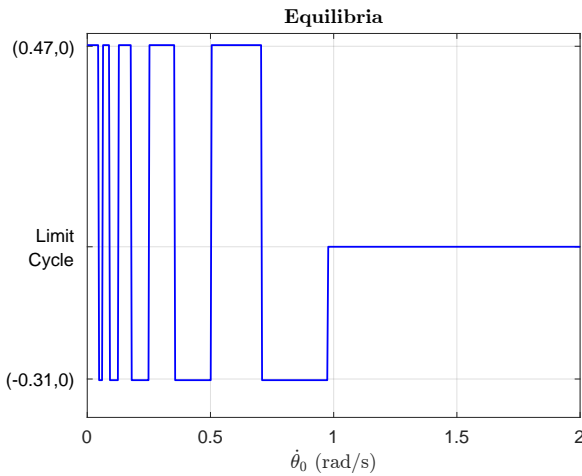


Figure 43: Positive values

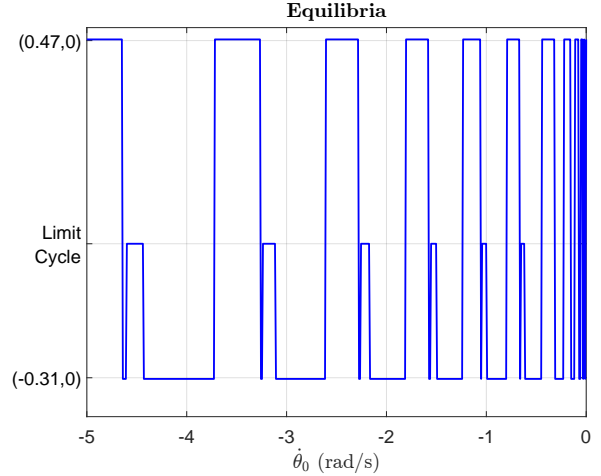


Figure 44: Negative values

For positive values, a key observation is that for values of $\dot{\theta}_0$ in the interval $(0, 0.97]$, the system converges to one of two alternating equilibrium points, located at $(-0.3127, 0)$ and $(0.4727, 0)$, respectively, depending on the specific initial velocity. In contrast, when $\dot{\theta}_0 \geq 0.98$, the system no longer converges to an equilibrium point but instead evolves toward a stable limit cycle. As $\dot{\theta}_0$ increases, the time required for convergence to the final behaviour (either equilibrium or limit cycle) also tends to increase. For negative initial velocities, the system exhibits high-frequency oscillations between the two equilibrium points and the limit cycle when the angular velocity is slightly negative. As the initial velocity decreases further, these oscillations tend to diminish. Moreover, both the number of initial values leading to a limit cycle and those leading to an equilibrium point increase.

The limit cycle was chosen over the second equilibrium point for visualization purposes, as it also reveals the system's behavior when starting from a negative initial velocity. In this scenario, the value of -5 —selected from the equilibrium plot—highlights the moment at which the rimless wheel's velocity reaches zero, marking a reversal in the direction of motion. The wheel initially ascends before descending, converting potential energy into kinetic energy. This energy accumulation ultimately enables the system to converge to a stable limit cycle.

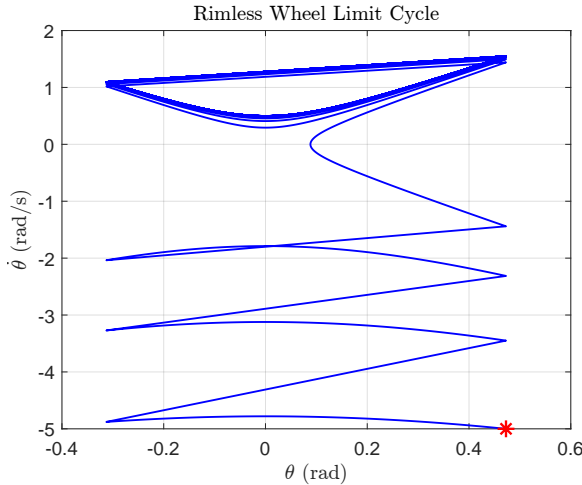


Figure 45: $\dot{\theta}_0 = -5$, $p_i = (0.47, -5)$

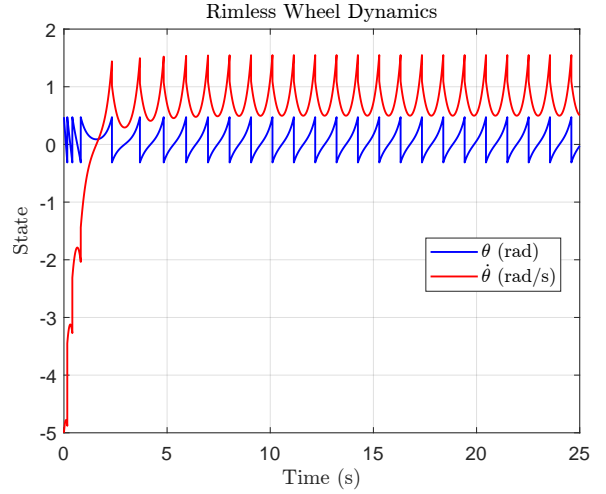


Figure 46: $\dot{\theta}_0 = -5$, $p_i = (0.47, -5)$

4.1 Rimless wheel with modified parameters.

In the first stage of the analysis, the slope inclination γ was progressively varied to study the system's behaviour. For inclination angles below the initial value, the system converges to equilibrium points. However, as γ increases beyond this value, limit cycles emerge and differ from the case in which $\gamma = 0.08$. The most notable observation from the simulations is that both the frequency and magnitude of the velocity and position oscillations increase with the slope angle, as a result of the greater kinetic energy acquired. To highlight this effect, two simulations were carried out with slope angles of 10° and 20° , respectively.

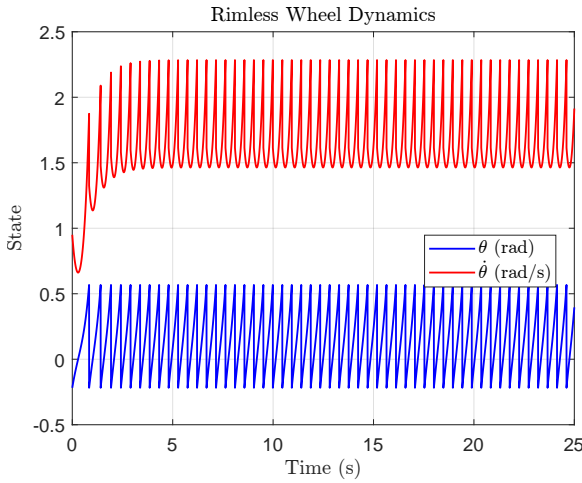


Figure 47: $\dot{\theta}_0 = 0.95$, $\gamma = 0.1746$ rad

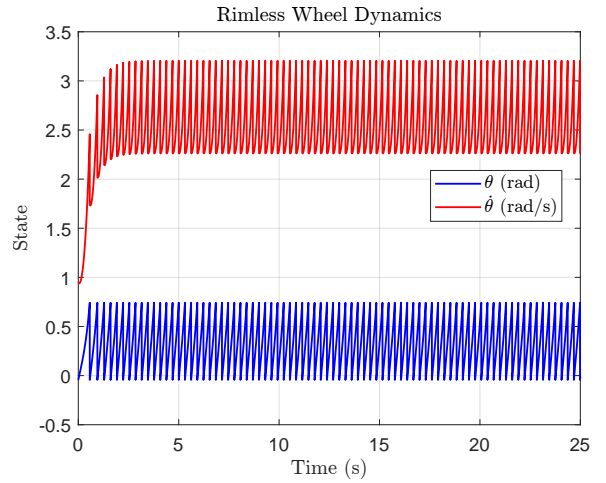


Figure 48: $\dot{\theta}_0 = 0.95$, $\gamma = 0.3491$ rad

By gradually varying the leg length, the same two equilibrium points observed in the initial case alternate for values below the threshold $l = 1.05$ m. However, beyond this threshold, different limit cycles emerge. As the leg length increases, both the frequency and amplitude of position and velocity oscillations tend to decrease. This behavior can be explained by the longer leg length, which increases the time interval between successive ground contacts.

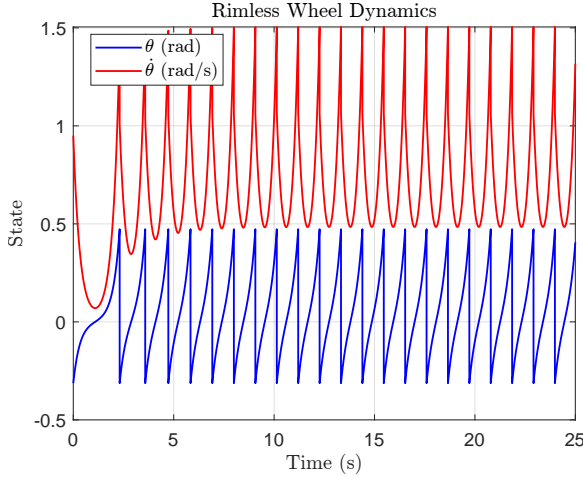


Figure 49: $\dot{\theta}_0 = 0.95$, $\gamma = 0.1746$ rad

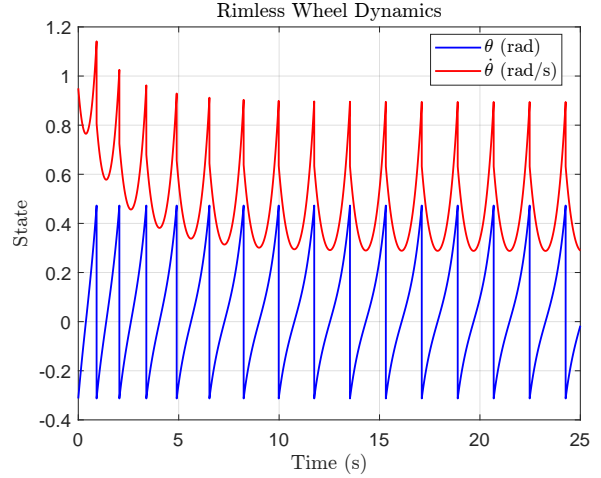


Figure 50: $\dot{\theta}_0 = 0.95$, $\gamma = 0.3491$ rad

The final parameter variation concerns the angular spacing between the legs, defined by the angle α , which determines the number of legs on the wheel. As α increases, the number of legs decreases and the ground contact duration of each leg shortens. For $\alpha > \frac{\pi}{8}$, the system converges to two equilibrium points; for smaller values, a limit cycles emerge due to more frequent ground contacts. To explore this behavior, two simulations were performed: one with 10 legs and one with 16.

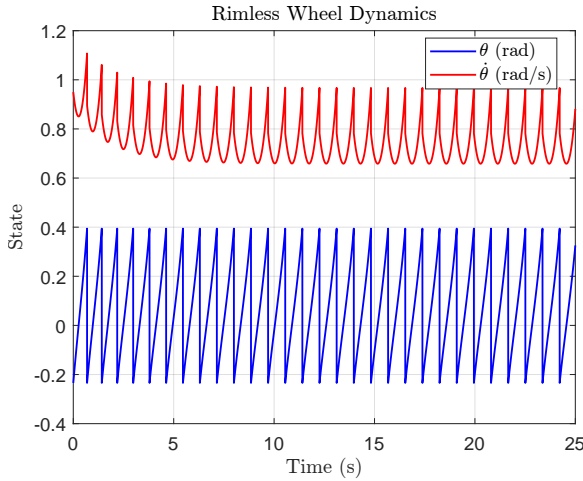


Figure 51: $\dot{\theta}_0 = 0.95$, $\alpha = \frac{\pi}{10}$

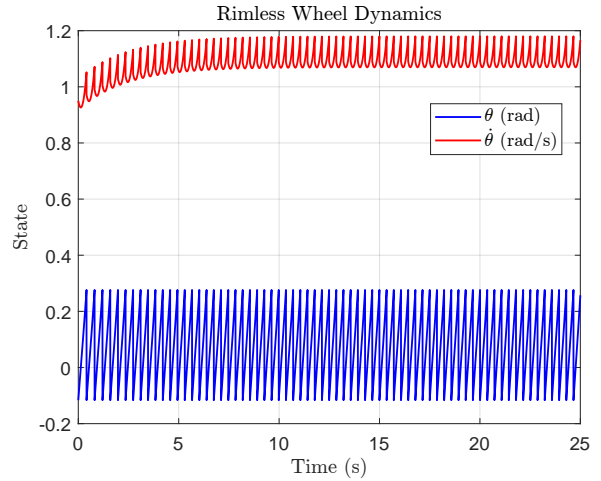


Figure 52: $\dot{\theta}_0 = 0.95$, $\alpha = \frac{\pi}{16}$

As α decreases, the oscillation frequency increases for both position and velocity. However, the magnitude of the position oscillations is greater for larger values of α , and decreases as α becomes smaller. In contrast, the velocity exhibits the opposite behavior: its oscillation magnitude increases as α decreases.